nature portfolio

https://doi.org/10.1038/s41567-022-01721-w

## Supplementary information

# Many-body dynamical delocalization in a kicked one-dimensional ultracold gas

In the format provided by the authors and unedited

# Supplementary Information for "Many-body Dynamical Delocalization in a Kicked 1D Ultracold Gas"

Jun Hui See Toh,[1] Katherine C. McCormick,[1] Xinxin Tang,[1] Ying Su,[2] Xi-Wang Luo,[2] Chuanwei Zhang,[2] and Subhadeep Gupta[1]

[1] *Department of Physics, University of Washington, Seattle, Washington 98195, USA*

[2] *Department of Physics, The University of Texas at Dallas, Richardson, Texas 75080-3021, USA*

## EXPERIMENTAL DETAILS

*Optical Lattice Implementations.*— The two-dimensional lattice potential is always applied such that each of the two arms contributes a peak (AC Stark) potential depth $V_{\rm lat}$. The overall lattice potential is then:

$$-V_{\rm lat}\left[\frac{e^{-\frac{2(y^2+z^2)}{w_x^2(1+x^2/x_R^2)}}}{1+x^2/x_R^2}\cos^2(k_L x)+\frac{e^{-\frac{2(x^2+z^2)}{w_y^2(1+y^2/y_R^2)}}}{1+y^2/y_R^2}\cos^2(k_L y)\right] \tag{S1}$$

where $j_R=\pi w_j^2/\lambda$ is the Rayleigh range along the $j^{\rm th}$ direction ($j$ is $x$ or $y$). The full depth of the lattice is $2V_{\rm lat}$. By taking the lowest order expansion of this expression in $x, y, z$, we obtain the radial and axial trap frequencies for the center tube located at the origin:

$$\omega_j=\sqrt{\frac{2V_{\rm lat}}{m}\left(\frac{2}{w_j^2}+\frac{1}{j_R^2}+k_L^2\right)}\simeq\sqrt{\frac{2V_{\rm lat}k_L^2}{m}}=2\omega_{\rm rec}\sqrt{s_\perp}=\omega_\perp,\quad \omega_z=\sqrt{\frac{4V_{\rm lat}}{m}(\frac{1}{w_x^2}+\frac{1}{w_y^2})}=2\frac{\lambda}{\pi\bar{w}}\omega_{\rm rec}\sqrt{s_\perp} \tag{S2}$$

where $2/\bar{w}^2=1/w_x^2+1/w_y^2$, $s_\perp=V_{\rm lat}/E_{\rm rec}$, $E_{\rm rec}=\frac{\hbar^2k_L^2}{2m}$ is the recoil energy and $m$ is the mass of an $^{174}$Yb atom. Since the lattice beam waists are much larger than the initial BEC size, all tubes containing atoms experience approximately the same trap frequencies.

We transfer the atoms from the ODT into about 570 horizontal tubes, as determined by the initial Thomas-Fermi radii in the 3D trap. The separation of individual tubes is below our imaging resolution, preventing access to accurate individual in-trap 1D TF profiles. We instead perform a Gaussian fit to the in-trap spatial distribution and measure an initial (tube-averaged) axial size of 27 $\mu$m for $s_\perp=106$. The atom number in the central tubes is about 650, and the peak density of the central tubes is then $\bar{n}_{\rm 1D}=24\,/\mu$m.

By observing the growth in the axial momentum distribution as the atoms are held in the lattice in the absence of kicking pulses, we determine the background heating rate for atoms trapped in 1D tubes. As shown in Fig. S1, for $s_\perp=106$, we measure a kinetic energy growth rate of $6\,E_{\rm rec}$/s.

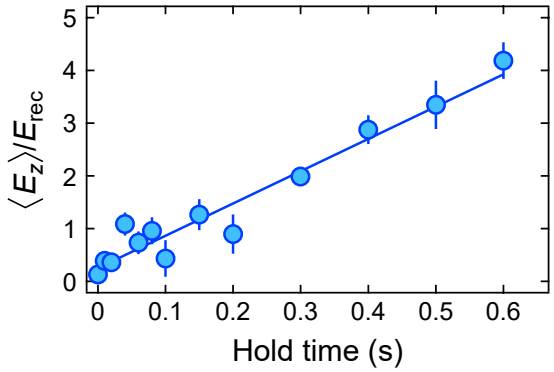


FIG. S1. **Background heating rate in lattice.** The plot shows the measured mean energy in the absence of pulses, after different hold times in a two-dimensional lattice of depth $s_\perp=106$. Also shown is the linear fit, which gives a background heating rate of $6\,E_{\rm rec}$/s, which is negligible on the timescale of the QKR experiments. Error bars show 1 s.e.m. (not visible when smaller than the marker size).

The kicking beam waist and Rayleigh range are much larger than the initial BEC size and we can express the kicking pulse potential as $V_{\rm kick}\cos^2(k_L z) = s_z E_{\rm rec}\cos^2(k_L z)$. As shown in Fig. 1b of the main text, even after 100 kicks with $s_z = 80$, when the axial delocalization has become significant, the transverse excitation is negligible at $< 10\%$. The 1D geometry also suppresses losses from three-body recombination [1]. Spontaneous scattering from lattice photons are also insignificant for our experimental parameters. Indeed atom loss in our 1D system only ensues when the QKR has reached a mean energy $\langle E_z\rangle$ of $10\,E_{\rm rec}$ for $s_\perp = 106$, due to the finite trap depth. This can be seen in Fig. S2, in comparison with the delocalization data presented in Fig. 3a of the main text.

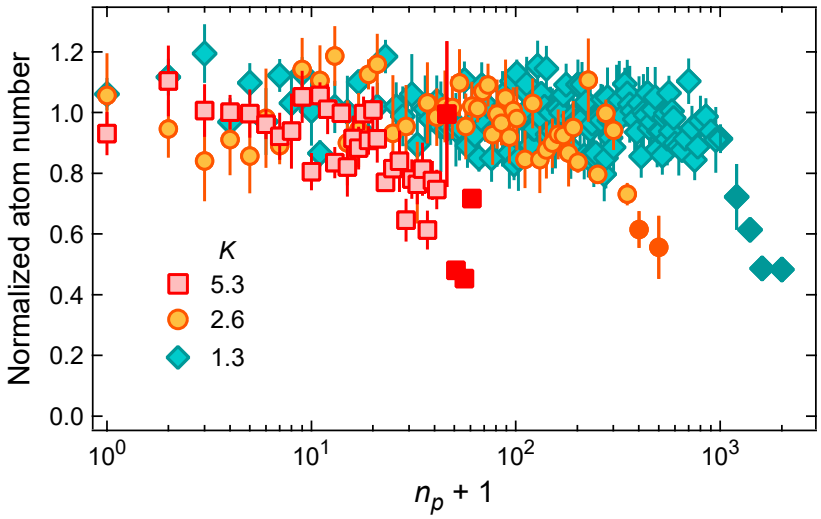


FIG. S2. **Atom number evolution during kicking process.** Normalized atom number as a function of pulse number $n_p$ for the data corresponding to the mean energy evolution presented in Fig. 3a in the main text. For each $K$, the darker colored markers (with the same shape) correspond to the largest pulse numbers that are not included in Fig. 3a of the main text. Error bars show 1 s.e.m. (not visible when smaller than the marker size).

*Analysis of the exponent, prefactor, and onset time of delocalization.*— To compare our observations against earlier theoretical results for QKR with interactions, we fit power law functions $E_0\tau^\alpha$ to our delocalization data, to obtain the prefactor $E_0$ and exponent $\alpha$ using the following procedure.

For each data set shown in Fig. 3 of the main paper, we first choose a range of starting and ending points for the fits (see Table I). For a particular dataset, we perform several power law fits, one for each pair of starting and ending points. We then determine values for $E_0$ and $\alpha$ for that dataset from the averages of all the values returned by the fits.

We choose our ranges of start and end points carefully, in order to guard against our lack of precise knowledge of how the delocalization starts and also from systematic effects specific to our experiment. The starting ranges are chosen to be after some delocalization is clearly observable in the data. The ending points are chosen such that they are below two experimental timescales: (a) time at which sharp atom loss is observed (see Fig. S2) and (b) the axial oscillation period (about $15.6\,\mu$s or 150 pulses with $T = 105\ \mu s$). For datasets (ii), (iv), (v), (vi), ending points of 110-130 are used because (a) precedes (b). For dataset (i), (b) precedes (a) (see Fig. S2), so the ending points only go up to 20 pulses. For dataset (i) the dominant energy growth happens after (b). Thus, even though we show a power law fit for dataset (i) in Fig 3 of the main paper, we do not include this in determining trends for delocalization versus our parameters.

Fig. S3 shows the sub-diffusive exponent $\alpha$ and prefactor $E_0$ (in units of $E_{\rm rec}$) versus $K$ and $gn_{\rm 1D}$ corresponding to the data shown in Figure 3 of the main paper. While the interaction-driven delocalization is clearly sub-diffusive ($\alpha < 1$), we do not find any clear trends of $\alpha$ with $K$ or $gn_{\rm 1D}$ within the parameter space explored. Mapping out the behavior of $\alpha$ over a larger region of QKR and interaction parameters is an interesting avenue for future investigation, but beyond the scope of this work.

The exact onset time of delocalization $n_p^*$ is difficult to determine as we lack precise knowledge of how it starts. We therefore define $n_p^*$ operationally, as when the energy reaches $2.5E_{\rm rec}$, a value where delocalization has clearly set in, as

TABLE I. **Ranges of pulse numbers used for fitting the data, corresponding energy ranges and number of fits.**

| Dataset | Figure | Beginning $n_p$ | Ending $n_p$ | Beginning $\langle E_z \rangle$ | Ending $\langle E_z \rangle$ | Number of fits |
|---|---|---|---|---|---|---|
| (i) | 3(a) $K = 1.3$ | 50-70 | 500-600 | $1.6 - 3.4 E_{\mathrm{rec}}$ | $8.0 - 9.8 E_{\mathrm{rec}}$ | 99 |
| (ii) | 3(a) $K = 2.6$ | 30-50 | 110-130 | $3.1 - 4.4 E_{\mathrm{rec}}$ | $7.7 - 10.1 E_{\mathrm{rec}}$ | 18 |
| (iii) | 3(a) $K = 5.3$ | 3-8 | 15-20 | $4.1 - 7.2 E_{\mathrm{rec}}$ | $8.2 - 11.3 E_{\mathrm{rec}}$ | 36 |
| (iv) | 3(b) $gn_{1\mathrm{D}} = 11.4$ | 30-50 | 110-130 | $1.6 - 2.4 E_{\mathrm{rec}}$ | $3.2 - 4.4 E_{\mathrm{rec}}$ | 30 |
| (v) | 3(b) $gn_{1\mathrm{D}} = 14.3$ | 30-50 | 110-130 | $2.3 - 3.1 E_{\mathrm{rec}}$ | $5.3 - 6.5 E_{\mathrm{rec}}$ | 36 |
| (vi) | 3(b) $gn_{1\mathrm{D}} = 18.7$ | 30-50 | 110-130 | $3.1 - 4.4 E_{\mathrm{rec}}$ | $7.7 - 10.1 E_{\mathrm{rec}}$ | 18 |

observed in the system energy evolution. We then use the fit values $E_0$ and $\alpha$ of the power function $E_0 \tau^\alpha = E_0 (n_p)^\alpha$ to solve for $n_p^*$. As shown in Fig. S3, the onset time of delocalization is earlier with stronger interaction strength and kick strength, as one would expect. We note that even though a choice different from $2.5 E_{\mathrm{rec}}$ discussed above would lead to different values of $n_p^*$, the trends versus $gn_{1D}$ and $K$ would not change.

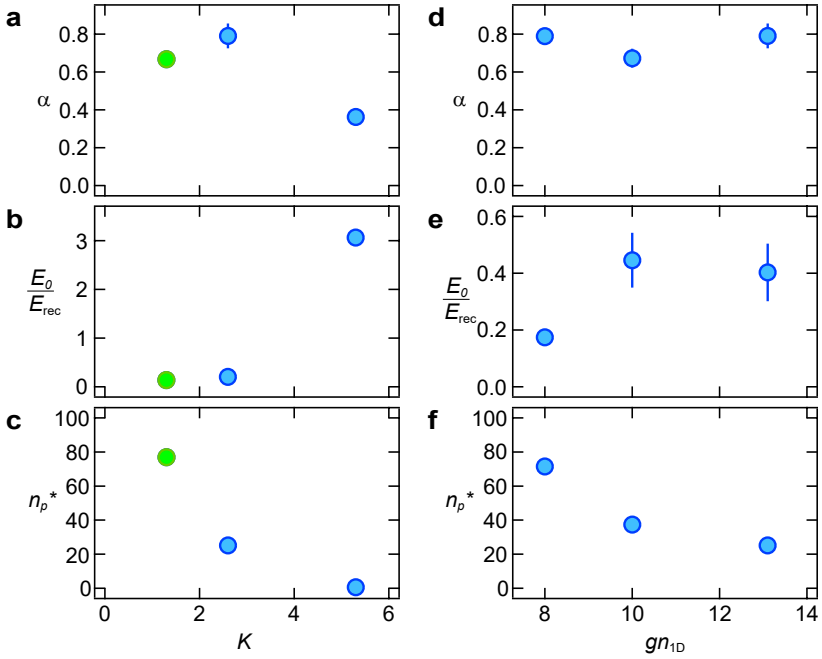


FIG. S3. **Analysis of the delocalization dynamics.** Exponent $\alpha$, prefactor $E_0$, and onset time of delocalization $n_p^*$ for the corresponding data in Fig. 3 in the main text. $K = 1.3$ data point is colored differently (green) to indicate that the fitting range of the data goes beyond the axial oscillation period. Error bars show 1 s.d. (not visible when smaller than the marker size).

*In-trap size during kicking.*— Since our QKR implementation is in a geometry that is not closed (such as a ring trap), we can expect that momentum diffusion will also lead to spatial diffusion. Shown in Fig. S4 are measured in-trap axial ($z$) and transverse ($y$) sizes (full-width-half-max) for the conditions corresponding to the $K = 2.6$ data in Fig. 3a of the main text, where mean energy evolution was presented. The measured in-trap axial size starts at $27\,\mu$m and indeed starts to grow after dynamical delocalization has set in (beyond 20 pulses). Fitting the growth part of Fig. S4 with a power law function of the form $z_0 \tau^\beta$ returns $\beta = 0.36(2)$. This would suggest a corresponding power-law growth of $2\beta$ for $\langle p^2 \rangle$ or $\langle E_z \rangle$ for these conditions, which is consistent with Fig. 3a of the main text. As expected, the transverse FWHM size does not change throughout the experiment and remains consistent with the initial TF radius in the $y$-direction.

*QKR with different pulse periods.*— Within the parameter space available in our experiment, we have observed dynamical delocalization over a large range of kick periods. Figure S5 shows the evolution of $\langle E_z \rangle$ for five period values in the range $T = 20\,\mu$s to $125\,\mu$s, with $t_p = 2\,\mu$s, while keeping the kick strength fixed at $K = 0.7$. We also note that the period value of $T = 125\,\mu$s corresponds to the quantum anti-resonance condition, where we would expect oscillatory behavior in the non-interacting case.

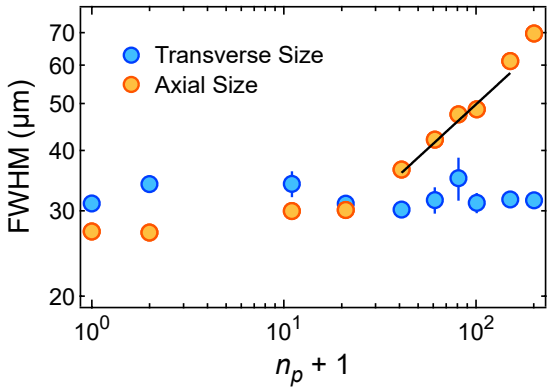


FIG. S4. **Evolution of cloud size during kicking process.** Axial ($z$) and transverse ($y$) size of the atom cloud confined in the $s_\perp = 106$ lattice versus pulse number with $s_z = 80$, $T = 105\mu$s, $K = 2.6$, $gn_{1D} = 18.7$. The transverse size does not change over the course of the experiment, while the axial size starts to grow after the onset of dynamical delocalization. The solid line is a power law fit to the growth part and returns an exponent value consistent with that observed in momentum space. Error bars show 1 s.e.m. (not visible when smaller than the marker size).

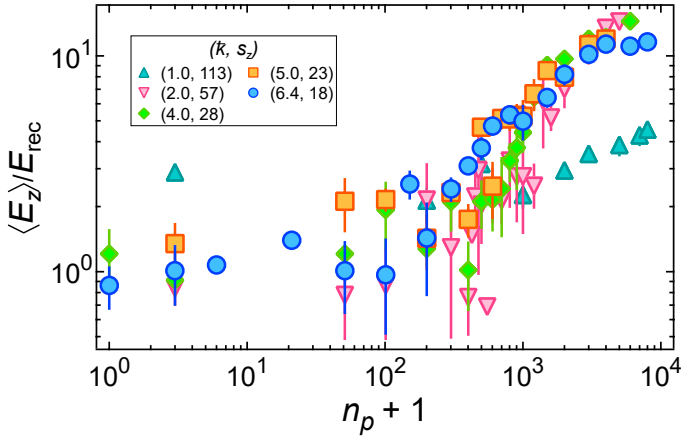


FIG. S5. **Onset of many-body dynamical delocalization for various kick periods.** Shown are mean energies as a function of pulse number for different kick periods $T$ (thus $\hbar$) and kick lattice depth $s_z$, while keeping the kick strength $K = 0.7$ constant. The kick periods used are $T = \{20, 40, 80, 100, 125\}\mu$s, corresponding to $\hbar = \{1.0, 2.0, 4.0, 5.0, 6.4\}$. Error bars show 1 s.e.m. (not visible when smaller than the marker size).

*Controlling interaction via atom number.*— In addition to the transverse confinement, the interaction strength in 1D tubes can also be tuned using the atom number $N_{\text{atom}}$ (thus $n_{1D}$). As shown in Fig. S6, we observe that the QKR behavior changes dramatically with change of initial $n_{1D}$ but keeping the same $g$. As before, the numerical GP solutions track our experimental observations reasonably well when far away from the delocalization-localization boundary, but show significant deviations near it. The larger amplitude oscillations in the numerics are a consequence of the shorter period in the kick pulse parameters $(t_p, T) = (3.5, 40)\,\mu$s compared to that in Fig.3 of the main paper.

For all of the QKR experimental data presented in this work, the tubes are oriented along the horizontal $z$ direction, with the exception of the data shown in Fig. S6, where the tubes are oriented along the vertical $x$ direction. In order to counter gravity during the kick pulses, the ODT is not extinguished, leading to the higher axial frequency of $2\pi \times 158\,$Hz, the quadrature sum of the ODT and two-dimensional lattice contributions. The many-body delocalization observed in Fig. S6 thus further demonstrates the generality of the observed phenomenon.

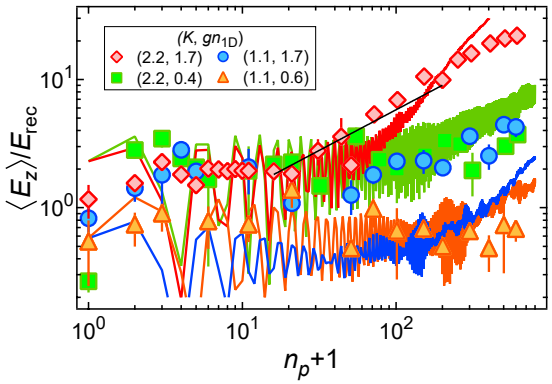


FIG. S6. **Tuning delocalization dynamics with number variation.** Shown are the evolution of mean energy for different number densities and kick strengths with $(t_p, T) = (3.5, 40)\,\mu$s, $k = 2.0$ in 1D tubes with $s_\perp = 106$, $g = 1.3$, and axial frequency $2\pi \times 161$ Hz. The colored solid lines are the corresponding numerical simulations using the GP equation and the black solid line is a power law fit to the delocalized data returning an exponent value of 0.63. Error bars show 1 s.e.m. (not visible when smaller than the marker size).

## THEORETICAL DESCRIPTION

*Gross-Pitaevskii Mean-field approach.*—As discussed in the main text, the transverse dynamics are suppressed by a strong two-dimensional lattice, and the system contains many nearly decoupled quasi-1D tubes. The Hamiltonian of each tube reads

$$\mathcal{H} = \int dz \hat{\Psi}(z)^\dagger [H_0 + \frac{\bar{g}}{2}\hat{\Psi}(z)^\dagger \hat{\Psi}(z)]\hat{\Psi}(z) \tag{S3}$$

with $\hat{\Psi}(z)$ the field operator of the Bose gas. The reduced 1D interaction strength is $\bar{g} = \frac{2\hbar^2 a_s}{m a_\perp^2}$, and the single-particle Hamiltonian is $H_0(t) = \frac{p^2}{2m} + V(z) - \hbar\kappa \cos(2k_L z)\sum_{n_p}\delta(t - n_p T)$, where $\hbar k_L$ is the recoil momentum, and the kick strength $\hbar\kappa = V_{\rm kick} t_p/2$. The dynamics of the nonlinear QKR are described by

$$i\hbar\partial_t \hat{\Psi}(z,t) = [H_0(t) + \bar{g}\hat{\Psi}(z,t)^\dagger \hat{\Psi}(z,t)]\hat{\Psi}(z,t). \tag{S4}$$

The regime of a Thomas Fermi (TF) condensate requires the correlation length $l_c = \frac{\hbar}{\sqrt{m\bar{g}\bar{n}_{\rm 1D}}}$ to be much larger than the mean inter-particle separation $1/\bar{n}_{\rm 1D}$, that is, the total atom number $N_{\rm atom}$ in each tube should be much larger than $N^* = (\frac{2a_s a_z}{a_\perp^2})^2$, with $a_z = \sqrt{\frac{\hbar}{m\omega_z}}$. Even for strong confinement along the transverse direction with $s_\perp = 106$, $N^* \simeq 15$. In our experiment, there are a few hundreds of atoms in each tube ($N_{\rm atom} \gg N^*$), therefore, the system is in the weakly interacting regime and we have a true TF condensate at low temperature [2]. In the opposite limit with $N_{\rm atom} \ll N^*$, the system would enter the Tonks gas regime.

As a result, we can write the field operator as

$$\hat{\Psi}(z,t) = \Phi(z,t) + \hat{\psi}(z,t), \tag{S5}$$

with $\Phi(z,t)$ the condensate wavefunction and $\hat{\psi}(z,t)$ the quantum fluctuation. To the zero-th order of $\hat{\psi}(z,t)$, we obtain the mean-field Gross-Pitaevskii (GP) equation

$$i\hbar\partial_t \Phi(z,t) = [H_0(t) + \bar{g}|\Phi(z,t)|^2]\Phi(z,t). \tag{S6}$$

*Hartree-Fock-Bogoliubov approach.*— Initially, our system is a true TF condensate with negligible fluctuations. As the kick number increases, the delocalization of the system may be accompanied with the rapid proliferation of non-condensate atoms, especially for strong interactions. The GP approach may apply only in the regime where the non-condensate particle number is much smaller than the condensate atom number. Therefore, it is important to go beyond the mean-field approach and examine the excitation properties. Here we employ the Hartree-Fock-Bogoliubov

approach to consider the effects of quantum fluctuation $\hat{\psi}(z,t)$ [3]. Substituting Eq. S5 into Eq. S4, and keeping the terms up to the second order of $\hat{\psi}(z,t)$, we obtain

$$i\hbar\partial_t\Phi(z,t) = [H_0(t) + \bar{g}|\Phi(z,t)|^2 + 2\bar{g}n']\Phi(z,t) + \bar{g}m'^*(z,t), \tag{S7}$$

with $n' = \langle\hat{\psi}^\dagger(z,t)\hat{\psi}(z,t)\rangle$, $m' = \langle\hat{\psi}(z,t)\hat{\psi}(z,t)\rangle$. The quantum fluctuation satisfies

$$i\hbar\partial_t\hat{\psi}(z,t) = [H_0(t) + 2\bar{g}(|\Phi|^2 + n')]\hat{\psi}(z,t) + \bar{g}(|\Phi|^2 + m')\hat{\psi}^\dagger(z,t). \tag{S8}$$

Using the Bogoliubov transformation

$$\hat{\psi}(z,t) = \sum_j u_j(z,t)\hat{\beta}_j - v_j^*(z,t)\hat{\beta}_j^\dagger, \tag{S9}$$

with $\hat{\beta}_j^\dagger$ the excitation creation operator, we obtain the Bogoliubov equation

$$i\hbar\partial_t \begin{pmatrix} u_j \\ v_j \end{pmatrix} = \begin{pmatrix} M_0 & M_1 \\ -M_1^* & -M_0 \end{pmatrix} \begin{pmatrix} u_j \\ v_j \end{pmatrix}, \tag{S10}$$

where $M_0 = H_0(t) + 2\bar{g}(|\Phi|^2 + n')$ and $M_1 = \bar{g}(|\Phi|^2 + m')$. We are only interested in the stability of the system (*i.e.*, whether the non-condensate particle number $n'$ increases exponentially), which can be determined even when $n'$ is much smaller than the condensate. Therefore, we can ignore the $n'$ and $m'$ in the above equations for simplicity [4].

*Mapping to nonlinear Anderson model.*—As discussed above, in the regime where the non-condensate atom number is small, the GP equation gives a good description of the nonlinear QKR. It is known that the non-interacting QKR can be mapped to the Anderson model, i.e, a one-dimensional lattice in momentum space with on-site disorders [5]. Here we briefly review the mapping and discuss the effects of interactions. The QKR is a Floquet system with $\mathcal{H}(t) = \mathcal{H}(t+T)$, therefore the wave function takes the form of $\Phi(z,t) = e^{-i\epsilon t}\phi(z,t)$ with periodic part $\phi(z,t) = \phi(z,t+T)$ and quasienergy $\epsilon$. Denoting $\phi_\pm(z)$ as the wave functions just after and before the kick, we have

$$\phi_+(z) = e^{i\kappa\cos 2k_L z}\phi_-(z). \tag{S11}$$

For $g = 0$, the free evolution between kicks yields

$$\phi_{-,j} = e^{i(\epsilon T - 4j^2 E_{\rm rec}T/\hbar)}\phi_{+,j}, \tag{S12}$$

where $\phi_{\pm,j} = \frac{1}{\sqrt{Z}}\int dz e^{i2jk_L z}\phi_\pm(z)$ are the $j-$th Fourier components of the wave function with system size $Z$. For simplicity we have neglected the harmonic trap. From the above two equations, we obtain the effective Anderson model

$$V_j\bar{\phi}_j + \sum_{j'\neq 0} K_{j'}\bar{\phi}_{j+j'} = \omega\bar{\phi}_j, \tag{S13}$$

with on-site disorder $V_j = \tan(\epsilon T/2 - 2j^2 E_{\rm rec}T/\hbar)$, hopping rates $K_j = \frac{1}{\sqrt{Z}}\int dz e^{i2jk_L z}\tan[\frac{\kappa}{2}\cos(2k_L z)]$, and energy $\omega = -K_0$. Here $\bar{\phi}_j = (\phi_{-,j} + \phi_{+,j})/2$.

In the presence of interactions, the free evolution between two kicks can be written as

$$i\hbar\partial_t\phi(z,t) = [\frac{p^2}{2m} - \hbar\epsilon + \bar{g}|\phi|^2]\phi(z,t). \tag{S14}$$

In the momentum space,

$$i\hbar\partial_t\phi_j(t) = \sum_{j'}\left[\left(\frac{4j^2\hbar^2k_L^2}{2m} - \hbar\epsilon\right)\delta_{j',0} + \frac{\bar{g}}{Z}\sum_{j_1}\phi_{j_1}^*\phi_{j_1-j'}\right]\phi_{j+j'}(t). \tag{S15}$$

We see that the contact interactions in real space become long-range interactions in momentum space, which lead to the delocalization in momentum space, as observed in experiments. We can split the interactions into two parts: the

diagonal interaction with $j'=0$ or $j'=j_1-j$, and the off-diagonal interaction with $j'\neq 0$ and $j'\neq j_1-j$. The free evolution becomes

$$\begin{aligned} i\hbar\partial_t\phi_j(t) = &\left(\frac{4j^2\hbar^2k_L^2}{2m}-\hbar\epsilon\right)\phi_j(t) \\ &+\frac{\bar{g}}{Z}\left(2N_{\rm atom}-|\phi_j|^2\right)\phi_j(t) \\ &+\frac{\bar{g}}{Z}\left[\sum_{j'\neq 0, j_1-j}\phi^*_{j_1}\phi_{j_1-j'}\right]\phi_{j+j'}(t). \end{aligned} \tag{S16}$$

The first line on the right-hand side of the above equation corresponds to the single-particle evolution, while the second and third lines correspond to diagonal interactions (which lead to on-site attraction) and off-diagonal interactions (which lead to infinite long-range hopping).

Due to the infinite long-range feature, it is hard to obtain the relation between $\phi_-$ and $\phi_+$ based on the non-linear free evolution. However, if we consider only the diagonal interaction, we can obtain the solution

$$\phi_{-,j} = e^{i[\epsilon T-4j^2E_{\rm rec}T/\hbar+\bar{g}(2N_{\rm atom}-|\phi_{+,j}|^2)T/Z\hbar]}\phi_{+,j}. \tag{S17}$$

The nonlinear Anderson model takes the same form as Eq. S13, while the on-site disorder becomes nonlinear with $V_j = \tan(\epsilon T/2-(2j^2E_{\rm rec})T/\hbar-\bar{g}N_{\rm atom}T/Z\hbar+\bar{g}T|\sum_{j'}\bar{\phi}_{j+j'}(K_{j'}+\delta_{j,j'})|^2/2Z\hbar)$. Though there is no analytical expression, the off-diagonal interaction induces effective infinite long-range hopping in the nonlinear Anderson model, which together with the diagonal interaction are responsible for the dynamical delocalization.

## NUMERICAL RESULTS

For our numerical simulation, we take $2\hbar k_L$ and $T$ as the momentum and time units. The GP equation becomes

$$i\hbar\partial_\tau\Phi(\theta,\tau) = [-\frac{\hbar^2\partial_\theta^2}{2}+V(\theta)-K\cos(\theta)\sum_{n_p}\delta(\tau-n_p)+g|\Phi(\theta,\tau)|^2]\Phi(\theta,\tau), \tag{S18}$$

where $\tau=t/T$, $\theta=2k_Lz$, $\hbar=8TE_{\rm rec}/\hbar$ and $K=\hbar\kappa=\hbar V_{\rm kick}t_p/2\hbar$ are dimensionless parameters. The harmonic confinement $V(\theta)=\frac{1}{2}\omega_\theta^2\theta^2$ is expressed in terms of the dimensionless trapping frequency $\omega_\theta=\omega_zT$. The dimensionless interaction strength is expressed as $g=2\bar{g}k_LT\hbar/\hbar=\hbar^2\frac{k_La_s}{(k_La_\perp)^2}$, and the wave function is normalized as $\int d\theta|\Phi(\theta,\tau)|^2=N_{\rm atom}$ where $N_{\rm atom}$ is the atom number per tube.

For $^{174}$Yb atoms, $k_L=2\pi/\lambda$ with $\lambda=1073$ nm, and we have $E_{\rm rec}=\frac{\hbar^2k_L^2}{2m}=\hbar\times 2\pi\times 1$ kHz and $a_s=5.55$ nm. The effective Planck constant $\hbar=5.26$ for $T=105\mu$s. The kick strength is $K\simeq 2.63$ (i.e., $\kappa\simeq 0.5$) for $V_{\rm kick}=80E_{\rm rec}$ and $t_p=2\mu$s. To match the experimental condition, we consider all 1D tubes created by the two-dimensional lattice potential Eq. (S1). The number of atoms in each tube can be estimated from the initial atom density of the 3D TF condensate in the ODT

$$n_{\rm 3D}(\boldsymbol{r}) = \frac{\mu}{\bar{g}_{\rm 3D}}\left(1-\frac{x^2}{R_x^2}-\frac{y^2}{R_y^2}-\frac{z^2}{R_z^2}\right), \tag{S19}$$

where $\mu=h\times 1.1$ kHz is the chemical potential, $\bar{g}_{\rm 3D}=4\pi\hbar^2a_s/m=2.7\times10^{-33}$ J$\cdot\mu$m$^3$ is the interaction strength, and $\{R_x,R_y,R_z\}$=$\{2.4,\ 22,\ 6.6\}$ $\mu$m are the TF radii in the ODT. Upon the implementation of the two-dimensional lattice potential, the atoms are trapped in the 1D tubes at the potential minima, as shown Fig. S7 (lower panel). For the $i$-th tube centered at $(x_i,y_i)$ in the transverse cross section, the number of atoms in the tube is

$$\begin{aligned} N_{\rm atom}(x_i,y_i) &= \int_{x_i-\frac{\lambda}{4}}^{x_i+\frac{\lambda}{4}}dx\int_{y_i-\frac{\lambda}{4}}^{y_i+\frac{\lambda}{4}}dy\int_{-z_i}^{z_i}dz\ n_{\rm 3D}(\boldsymbol{r}) \\ &= \frac{\mu}{\bar{g}_{\rm 3D}}\left[\frac{z_i\lambda^2}{2}-\frac{z_i\lambda(48x_i^2\lambda+\lambda^3)}{96R_x^2}-\frac{z_i\lambda(48y_i^2\lambda+\lambda^3)}{96R_y^2}-\frac{z_i^3\lambda^2}{6R_z^2}\right], \end{aligned} \tag{S20}$$

where $z_i=R_z\sqrt{1-x_i^2/R_x^2-y_i^2/R_y^2}$ and $n_{\rm 3D}(x_i,y_i,|z|\geq z_i)=0$. The distribution of atom numbers among all tubes is shown in Fig. S7 (upper panel), where tubes are centered in the plaquettes. The red ellipse is the boundary of the 3D

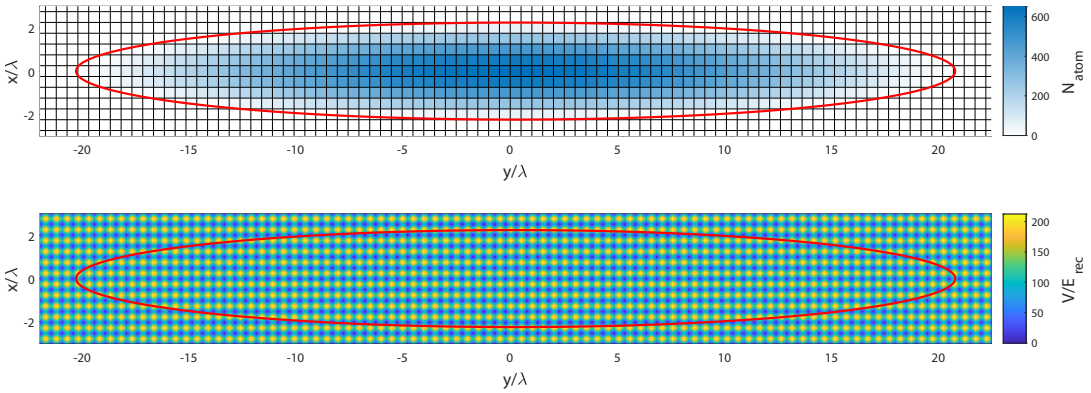


FIG. S7. **Number of atoms in each tube.** Upper panel shows the number of atoms in each 1D tube that is located at the center of each plaquette. Lower panel shows the two-dimensional lattice potential described by Eq. (S1) with $s_\perp = 106$ in the transverse cross section at $z = 0$ and the 1D tubes are created at the potential minima. The red ellipse is the boundary of BEC in the ODT before the implementation of the two-dimensional lattice potential.

TF condensate in the cross section at $z = 0$. The number of tubes can be estimated as $N_{\rm tube} = \pi R_x R_y/(\lambda/2)^2 \simeq 570$ and the averaged atom number per tube is $N_{\rm atom} \sim 300$. Furthermore, we use a Gaussian trap as depicted by Eq. (S1) in the axial direction, that is same as that in the experiment, whose low-energy small $\theta$ expansion leads to the harmonic trap $V(\theta)$.

We solve the GP equation Eq. (S18) numerically using the time-split method, with the initial state obtained by the imaginary time evolution of the time-independent GP equation without kicks. The initial state shows good agreement with the TF approximation, i.e., $|\Phi(\theta)|^2 = \frac{\mu - V(\theta)}{g}$, and the chemical potential $\mu = g n_{\rm 1D}$ where $n_{\rm 1D} = |\Phi(0)|^2$ is the peak density in the 1D tube. The chemical potential can be determined by the conservation of atom number $N_{\rm atom} = \int d\theta |\Phi(\theta)|^2$ that yields

$$g n_{\rm 1D} = g^{\frac{2}{3}} \left( \frac{9 N_{\rm atom}^2 \omega_\theta^2}{32} \right)^{\frac{1}{3}}, \tag{S21}$$

which characterizes the interaction strength. We simulate all 1D tubes with different atom numbers independently and the temporal evolution of mean energy (obtained by averaging over all 1D tubes which is weighted by different atom numbers) are shown in Fig. 3 of the main text. Here we adopt the experimental parameters given in Fig. 3a and 3c of the main text. The $g n_{\rm 1D}$ values quoted in Fig. 3c are the weighted average values over all 1D tubes.

Our numerical simulations show good agreement with the experimental data for parameters deep in the delocalization/localization regime, while around the localization-delocalization phase boundary, we observe large deviations between the simulation and experiment. This is because the dynamics become more sensitive to the parameters and the initial states (e.g., the numerical simulation starts with the ground state of the BEC while the initial state in the experiment may contain a small portion of excited states).

The numerical phase diagram in the $K$-$g n_{\rm 1D}$ plane is shown in Figure S8 (same as Fig. 3e of the main text). Here the phase transition points marked by the blue and red squares are obtained by solving the GP and Hartree-Fock-Bogoliubov equations, respectively. For the phase diagram, instead of simulating all 1D tubes with different atom numbers, here we consider a single 1D tube with the averaged atom number $N_{\rm atom} = 300$. The phase boundaries marked by the blue solid and red dashed lines are obtained by fitting to the phase transition points. Due to the dynamical localization in the absence of interaction, the phase transition point goes to infinity as $g$ decreases to zero. We find that the critical kick strength $K_c$ shows a roughly linear dependence on $(g n_{\rm 1D})^{-1}$, therefore we use the ansatz $y = a x^{-1} + b$ to fit the numerical results. The fitting parameters are $a = 24.95$ and $b = -0.12$ for the blue solid line, and $a = 26.34$ and $b = 0.14$ for the red dashed line. Above the blue solid line, the mean energy starts to increase with the pulse number, as shown in Figure S9, indicating the dynamical delocalization. The red dashed line corresponds to the boundary between stable and unstable regimes. Above the red dashed line, the BEC becomes unstable as kick number increases, which is manifest by the exponential increase of noncondensed atom number, as shown in Figure S10. The critical kick strengths ($K_c$) for both phase transitions decrease with $g n_{\rm 1D}$. We notice that the two phase boundaries are close to each other, which suggests that the dynamical delocalization is accompanied by the instability of the BEC.

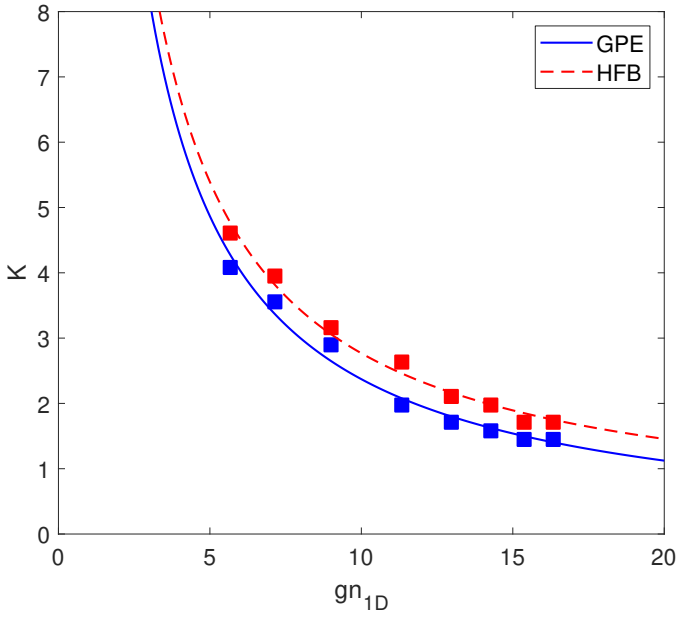


FIG. S8. **Phase diagram of the localization behavior of the system in the space of kick strength and interaction strength.** The blue and red markers are the phase transition points obtained by solving the GP and Hartree-Fock-Bogoliubov equations, respectively. The system is localized and stable below the markers, and delocalized and unstable above the markers. The phase boundaries marked by the blue solid and red dashed lines are the same as those in Fig. 3e of the main text and are obtained by fitting to the markers. Here we use the ansatz $y = ax^{-1} + b$ for the fitting. The fitting parameters are $a = 24.95$ and $b = -0.12$ for the blue solid line, and $a = 26.34$ and $b = 0.14$ for the red dashed line.


[1] B. L. Tolra, K. M. O'Hara, J. H. Huckans, W. D. Phillips, S. L. Rolston, and J. V. Porto, Observation of reduced three-body recombination in a correlated 1d degenerate bose gas, Phys. Rev. Lett. **92**, 190401 (2004).

[2] D. S. Petrov, G. V. Shlyapnikov, and J. T. M. Walraven, Regimes of quantum degeneracy in trapped 1d gases, Phys. Rev. Lett. **85**, 3745 (2000).

[3] A. Griffin, Conserving and gapless approximations for an inhomogeneous bose gas at finite temperatures, Phys. Rev. B **53**, 9341 (1996).

[4] C. Zhang, J. Liu, M. G. Raizen, and Q. Niu, Transition to instability in a kicked bose-einstein condensate, Phys. Rev. Lett. **92**, 054101 (2004).

[5] S. Fishman, D. R. Grempel, and R. E. Prange, Chaos, quantum recurrences, and anderson localization, Phys. Rev. Lett. **49**, 509 (1982).

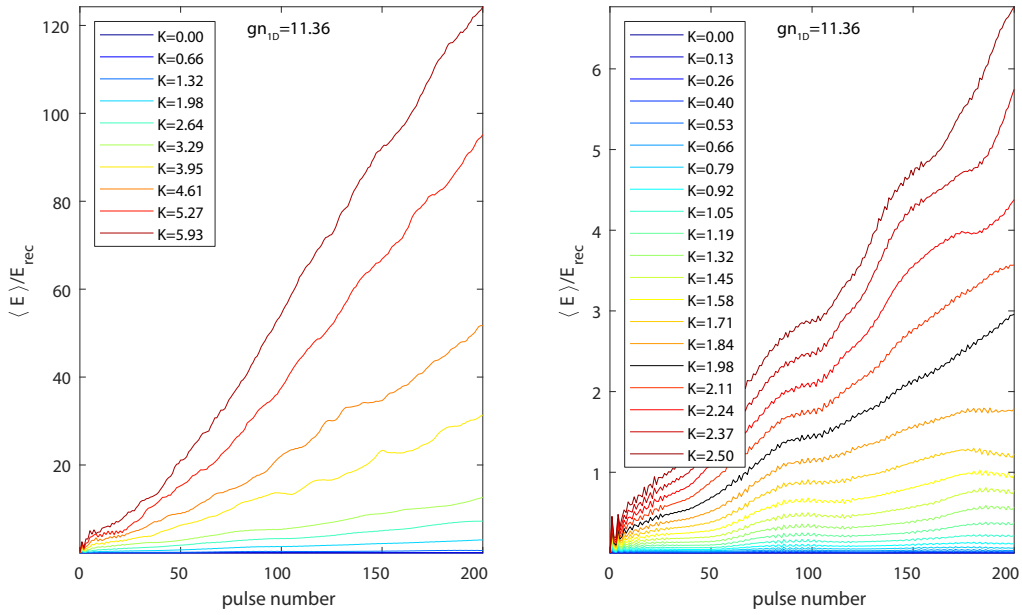


FIG. S9. **Mean energy as a function of pulse number for different $K$ with $gn_{\mathbf{1D}} = 11.36$.** In general, the energy increases faster for stronger kicks $K$ (left panel). In the localized phase, the energy saturates at a small value as the kick number increases, while in the delocalized phase, the energy increases diffusively with the kick number (right panel). Here $\hbar = 5.26$. The black line marks the critical kick strength $K_c$.

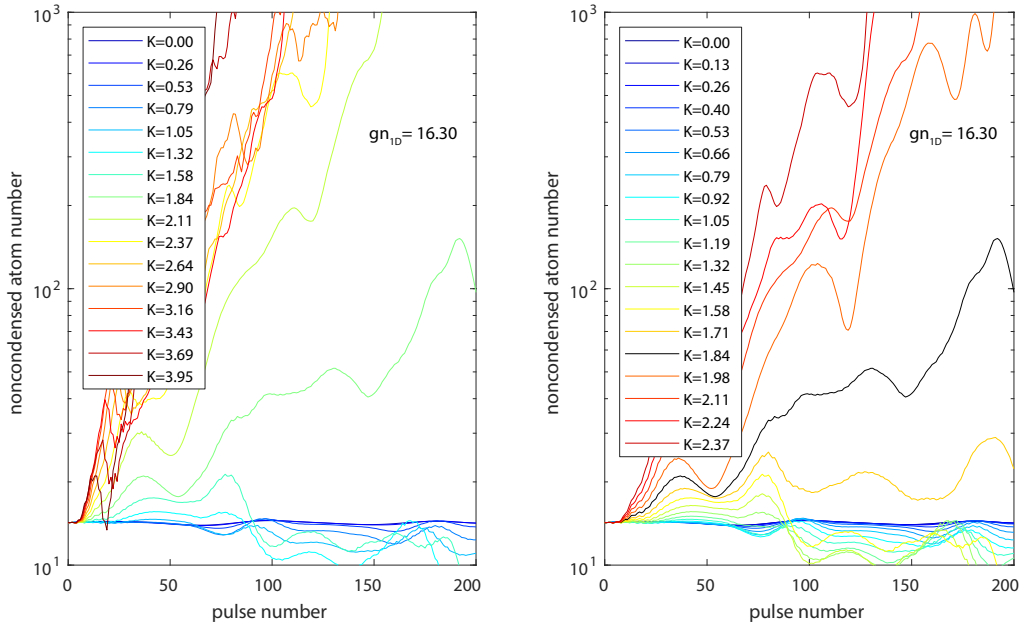


FIG. S10. **Noncondensed atom number as a function of pulse number for different $K$ with $gn_{1\mathrm{D}} = 16.3$.** At large kick number, the BEC becomes unstable as the interaction strength increases. The transition to instability happens around the transition to delocalization. Here the black line marks the critical kick strength $K_c$.